Front. Struct. Civ. Eng. 2023, 17(6): 855–869
https://doi.org/10.1007/s11709-023-0972-z

RESEARCH ARTICLE

Performance-based seismic assessment of a historical masonry arch bridge: Effect of pulse-like excitations

Amirhosein SHABANI[a], Mahdi KIOUMARSI[a*], Vagelis PLEVRIS[b]

[a] *Department of Built Environment, Oslo Metropolitan University, Oslo 0166, Norway*
[b] *Department of Civil and Architectural Engineering, Qatar University, Doha 2713, Qatar*
[*] *Corresponding author. E-mail: mahdi.kioumarsi@oslomet.no*

ABSTRACT Seismic analysis of historical masonry bridges is important for authorities in all countries hosting such cultural heritage assets. The masonry arch bridge investigated in this study was built during the Roman period and is on the island of Rhodes, in Greece. Fifteen seismic records were considered and categorized as far-field, pulse-like near-field, and non-pulse-like near-field. The earthquake excitations were scaled to a target spectrum, and nonlinear time-history analyses were performed in the transverse direction. The performance levels were introduced based on the pushover curve, and the post-earthquake damage state of the bridge was examined. According to the results, pulse-like near-field events are more damaging than non-pulse-like near-field ground motions. Additionally the bridge is more vulnerable to far-field excitations than near-field events. Furthermore, the structure will suffer extensive post-earthquake damage and must be retrofitted.

KEYWORDS masonry arch bridges, seismic behavior, modal properties, pulse-like records, nonlinear time history analysis

1 Introduction

Masonry arches are one of the earliest structural forms that have been used for thousands of years as parts of structures such as bridges and cathedrals [1]. It is widely accepted that the use of the arch as a structural form was developed independently in China and the Middle East more than 5000 years ago [2]. Masonry arch bridges still play a crucial role in transportation infrastructure in European countries because they form a significant part of the road and railway bridge inventory [3]. Historical masonry arch bridges must be preserved because of their importance as cultural heritage assets that carry lessons from past generations, in addition to their functional value as important infrastructure. Historical masonry arch bridges have been exposed to material degradation, scouring effects on boundary conditions, and changes in applied loads during their lifetime. In addition, they have been exposed to exceptional natural hazards such as earthquakes and floods. Furthermore, they were not originally built for the heavy loads they are often exposed to currently, and there are serious concerns about their safety for our society today [4].

Numerical modeling is an important part of seismic vulnerability assessment methodology [5,6]. The seismic vulnerability of masonry arch bridges must be assessed, because of the vulnerability of masonry subjected to earthquakes. Several different modeling strategies have been proposed for the simulation of the behavior of masonry arch bridges exposed to seismic events. Finite element (FE) modeling has been widely used to model masonry arch structures [3]. Using one-dimensional frame elements is the simplest approach for modeling masonry arch structures [7,8]. However, the effect of spandrel side walls and backfill soil material cannot be considered, and to tackle this limitation, nonlinear springs or nonlinear truss elements need to be used to simulate the interaction between the backfill, spandrel walls, and adjacent arches [9]. Two-dimensional (2D) FE models have also been used to explicitly model the fill soil and spandrel walls with higher computational effort compared with the one-dimensional modeling approach [10,11].

Article history: Received Sep 19, 2022; Accepted Dec 26, 2022

Finally, as the most detailed and complex method, three-dimensional (3D) FE modeling has been proposed, with detailed 3D modeling of all different parts of a bridge and the assignment of nonlinear constitutive relationships to both masonry and fill soil [12,13].

However, the considerable uncertainties related to the fill-structure interactions are possible limitations of the 3D FE modeling approach for masonry arch bridges. Contact interface elements (CIEs) were used comprising zero-thickness plane interface elements with normal and tangential stiffnesses derived based on the equations proposed for discrete element modeling of masonry structures [14,15]. A comprehensive study to investigate the effect of CIEs was performed, which emphasized the significant effect of CIEs on the modal properties as well as on the seismic behavior of a bridge [14]. A strategy was proposed to model a plane CIE with high normal stiffness to avoid the interpenetration of masonry and soil media such that no tension stiffness is considered [4,16,17]. Therefore, the CIE transfers only the compression and shear forces. Normal stiffness can be derived based on the soil−structure interaction equations, and the tangential stiffness is considered as 0.01–0.1 times the calculated normal stiffness [18,19]. However, the Coulomb friction model can also be used for a CIE with zero cohesion and friction coefficients [4,16,17].

Several studies have shown that structures subjected to near-field (NF) seismic events typically exhibit higher levels of damage owing to the strong velocity pulses of the excitations [20–22]. The results of linear time-history analysis of a two-span masonry bridge by applying one far-field (FF) and one NF event revealed that, in general, NF events cause more destructive damage than FF events [23]. However, by comparing the seismic response of a single-span masonry bridge subjected to FF and NF seismic events, it was concluded that the bridge is more susceptible to FF events [24]. This conclusion was further confirmed by performing linear seismic analyses on a single-span masonry bridge considering the soil−structure interaction [25]. Furthermore, similar results were obtained by performing a comparative study on a three-span masonry bridge by applying a set of eight FF and NF seismic events [26]. This finding is consistent with the conclusions drawn for nuclear structures [27].

Pulse-like near-field (PL-NF) ground motions are often caused by forward-directivity effects, and several different quantitative methods have been proposed for identifying pulse-like ground motions [28–31]. Studies have revealed that pulse-like events impose more significant demands on structures than non-pulse-like near-field (NPL-NF) seismic excitations [32–34]. However, these records cannot be labeled as aggressive without reference to structural characteristics [35]. Therefore, there is still a gap regarding the need to investigate the influence of PL-NF earthquake excitations on the seismic behavior of masonry arch bridges and compare the effect of FF and NF seismic excitations by applying a large number of events with several different characteristics.

2 Methodology and case study overview

In this study, the modeling procedure of a case study, the Roman Bridge located on the island of Rhodes, in Greece, was developed. The 3D geometric documentation was conducted using digital images, laser scanners, and total stations. The dimensions were obtained from the 3D product of geometric documentation. Using these data, an FE model was developed.

In the first part of the study, a dynamic modal analysis was performed, and the model was calibrated using an analytical equation to derive the first natural frequency value of masonry bridges.

As the examined bridge structure is located in a high seismicity zone, the second part of the study focused on investigating the seismic behavior of the bridge. To this end, 15 seismic events were selected that were categorized as FF, PL-NF, and NPL-NF. The records of these seismic events were scaled to a target response spectrum, and nonlinear time-history analyses (NLTHAs) were performed by applying the scaled seismic records in the transverse direction to assess the seismic vulnerability of the bridge. Three performance levels were calculated based on the pushover curve of the bridge, and the values of displacement capacity and demand were compared to assess the bridge performance levels.

The Roman Bridge, illustrated in Fig. 1 is located on the island of Rhodes, in Greece. It was built across the Rhodini stream before its outfall into the Mediterranean Sea at the main exit of the city on the east coast of the island. The bridge is 38.85 m long, 8.4 m wide, with a thickness of 0.6 m for the arch and spandrel components. The arch span is 6.4 m, and the height of the bridge is 5.2 m. Bridge building was a key part of the underlying Roman infrastructure [36,37], and the studied stone masonry bridge dates back to the Roman period. It is one of the few existing ancient bridges that still survive in Greece and remains in continuous use today. Later, repairs to the spandrel walls were reported, and temporary wooden scaffolds were built beneath the arches owing to falling stones. The island of Rhodes is in a high seismicity zone with peak ground acceleration (PGA) from 0.35g to 0.55g with 10% probability of

Fig. 1 Roman Bridge located on the island of Rhodes, in Greece.

exceedance in 50 years, equivalent to a return period of 475 years [38]. Documentation also reveals that several earthquakes have occurred in the island region, some of which are also associated with tsunamis [39,40]. For this purpose, the seismic vulnerability of the Roman Bridge as a cultural heritage asset and infrastructure must be assessed.

3 Numerical modeling

3.1 Three-dimensional geometric documentation

Geometric documentation is crucial for developing detailed and accurate 3D simulation models [41]. Geodetic, photogrammetric, and laser scanning data acquisition methods were used to provide an accurate 3D model of the bridge. In total, 2576 aerial images from drones and 271 ground digital images were processed using image-based modeling software to develop the 3D dense point cloud of the case study. The aerial images (using drones) were processed separately from the ground images because they had a lower resolution. Furthermore, 24 scans were performed using 3D laser scanners to provide point clouds to fill the gaps in 3D dense point clouds derived from the digital images. A local reference coordinate system was established using two total stations, and the coordinates of the required points, such as targets for the point cloud registration and ground control points for the orientation of the images, were determined. The workflow for obtaining the final 3D point cloud is illustrated in Fig. 2. Further details regarding this methodology can be found in the literature [42,43].

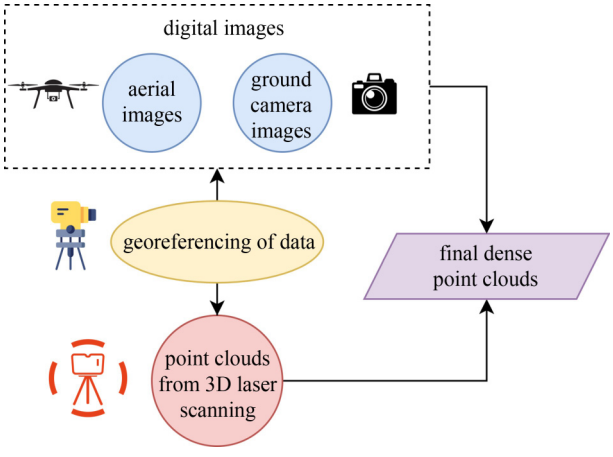

Fig. 2 Workflow of holistic methodology for generating final 3D point clouds.

After providing the final 3D point clouds, the triangular irregular network method was used to represent continuous surfaces. The light 3D model of the bridge shown in Fig. 3(a) was developed by reducing the number of triangular meshes without compromising the surface detail or color. Furthermore, cross sections were produced with different interval distances, as illustrated in Fig. 3(b). A 3D light model was used for visualization, and the dimensions of the bridge were determined from both products [44].

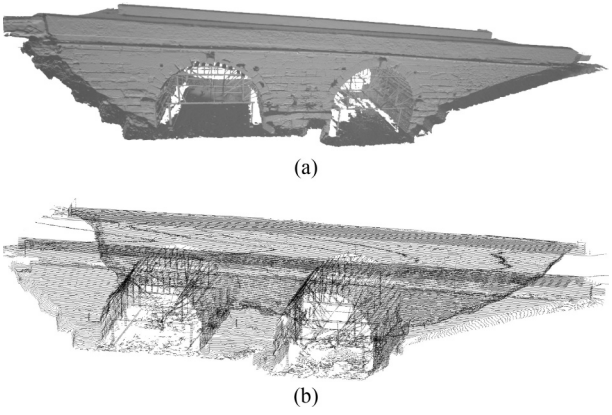

Fig. 3 (a) 3D light model; (b) cross sections of the bridge.

3.2 Three-dimensional finite element modeling

The geometry of the bridge was obtained from the 3D models used to develop the 3D FE model with DIANA FEA software [45]. Masonry is a construction material with complex mechanical behavior [46], and in the discrete element modeling approach, masonry units and mortar are modeled separately by means of interface elements to decrease the corresponding uncertainties [47]. For 3D FE modeling of the masonry part of the bridge, the homogenized method was used in which the discretization of the masonry units and mortar was ignored, which is widely used as a simplistic approach for modeling full-scale unreinforced masonry structures [48]. This approach requires less input data and computational effort than the discrete element method [49]. Figure 4(a) illustrates the different parts of the masonry arch bridge comprising spandrel walls, arches, and parapets made of stone masonry and backfill soil. To model the backfill-spandrel and backfill-arch interaction, CIEs were used, as shown in Fig. 4(b), as described previously [50]. The effect of soil−structure interaction was not considered, and rigid boundary conditions were set for the models.

The CIE can transfer normal compression and tangential friction with zero tensile strength; thus, the tensile forces are not transferred. Modeling the CIE is recommended not only to represent the actual behavior of the bridge but also to avoid early convergence problems owing to the low stiffness of the backfill material compared with the stiffness of the masonry material [4]. Nevertheless, the higher computational effort and level of input data and the additional need for a skilled analyst to model the CIE can be considered as limitations of

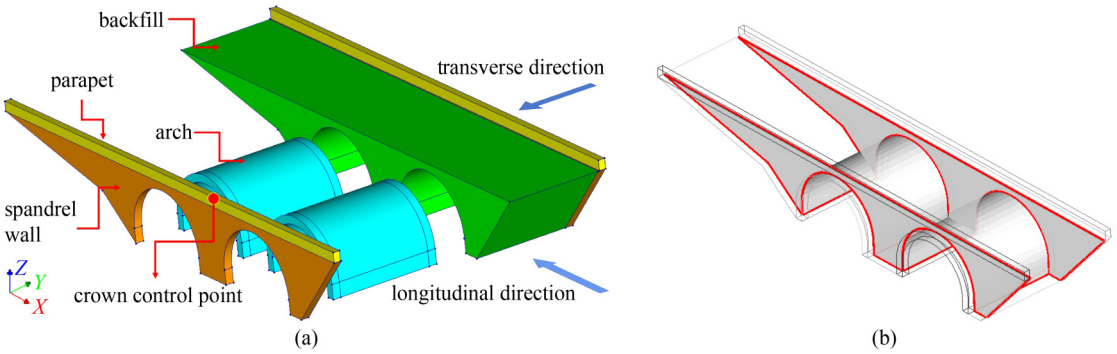

Fig. 4 (a) Different components of the numerical model of the Roman Bridge and loading directions in addition to the location of control (crown) point; (b) CIE used to model the bridge.

modeling masonry arch bridges using the CIE.

A high value was considered for the normal and lateral stiffnesses of the CIE to prevent the interpenetration of the two bodies. The CIEs follow the Coulomb friction model in such a way that the two media can carry shear stresses up to a certain magnitude, τ_{max} calculated using Eq. (1), before sliding across one another

$$\tau_{max} = c + \sigma \tan \varphi, \tag{1}$$

where c is the cohesion value (considered to be zero), σ is the normal stress, and φ is the friction angle of the soil. The friction coefficient (tangent of the friction angle) is recommended to be in the range of 0.4–0.5 [51–53].

3.3 Material properties

The total strain fixed crack model was applied for the nonlinear modeling of the masonry parts to define the tensile and compressive behaviors of the homogenized stone masonry with a single stress−strain relationship [54]. The area under the exponential softening curve is calculated based on the tension fracture energy (G_f^t) divided by the definition of the crack bandwidth (h) of an element. For the compression part, the area under the parabolic curve is calculated based on the compression fracture energy (G_f^c) divided by h to define the stress−strain curve of the masonry, as shown in Fig. 5. Note that the crack bandwidth model was used in this study, and parameter h is related to the volume of the element [55].

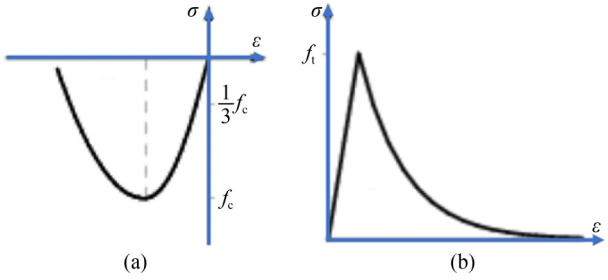

Fig. 5 Uniaxial stress−strain diagrams of homogenized stone masonry: (a) compression behavior; (b) tension behavior.

The damage-based shear retention model was selected for the masonry shear behavior. The shear retention was simulated based on the material damage caused by cracking, and the shear capacity was reduced to zero when the masonry was sufficiently damaged. The bridge is made of "sfouggaria stone", which was a common construction material on the island of Rhodes in the past, with a compressive strength (f_b) estimated at 9 MPa [56]. Moreover, the compressive strength of mortar (f_m) is considered to be 1 MPa by choosing a soft mortar type [57], owing to the presence of mildly leached mortar that can be raked out. The recommended equations and corresponding values for the material properties of the bridge masonry used in this study are listed in Table 1.

Moreover, the Mohr−Coulomb material model was selected for the simulation of the backfill soil. The corresponding material properties are presented in Table 2

Table 1 Equations recommended for calculating the mechanical properties of the homogenized unreinforced masonry [57] with the corresponding values calculated for the Roman Bridge case study

parameter	description	equation	value for the bridge
f_c	compressive strength (MPa)	$0.6 f_b^{0.65} f_m^{0.35}$	2.503
f_t	tensile strength (MPa)	$(10\%–20\%) f_c$	0.375
E	modulus of elasticity (GPa)	$(300–700) f_c$	1.001
G_f^c	fracture energy in compression (for the f_c lower than 12 MPa) (N·mm^{-1})	$1.6 f_c$	4.004
G_f^t	fracture energy in tension (N·mm^{-1})	$0.029 f_c$	0.011
ρ	density (kg·m^{-3})	–	2200
ν	Poisson's ratio	–	0.29

Table 2 Mechanical properties of the backfill soil

parameter	description	value
E_{bs}	modulus of elasticity (GPa)	0.3
ρ_{bs}	density (kg·m^{-3})	2000
ν_{bs}	Poisson's ratio	0.3
c_{bs}	cohesion (kPa)	10
φ_{bs}	friction angle of the backfill soil (°)	37
$f_{t(max)}$	tensile strength (kPa)	10

[58]. The friction coefficient value of the CIE was considered to be 0.4.

3.4 Finite element mesh

A preliminary analysis to assess the optimal mesh dimensions was performed on the FE model, and an adaptive mesh size of 0.5 m was used. Moreover, to simulate deformation across the arches accurately enough, a mesh size of 0.3 m was used for the arches. The 8-node quadratic element was selected for the FE modeling, which is the dominant type of element for such simulations. Tetrahedral volume elements were also used in the model to fill parts of the geometry. The FE mesh of the bridge is shown in Fig. 6. The model with the CIE is composed of 12699 mesh elements, of which 1936 are CIE elements.

4 Modal analysis and validation

Modal analysis was performed to derive the first five natural frequencies and corresponding mode shapes of the structure. The direction-dependent participation factors and modal mass percentages were also calculated for each natural mode and are presented in Table 3.

The first five modes with relatively high participation factor values were selected to perform the sensitivity analyses. Figure 7 shows the natural frequency values and corresponding mode shapes with a contour map of the normalized displacement values of the mode vectors of the first five modes of the model. Based on the results in

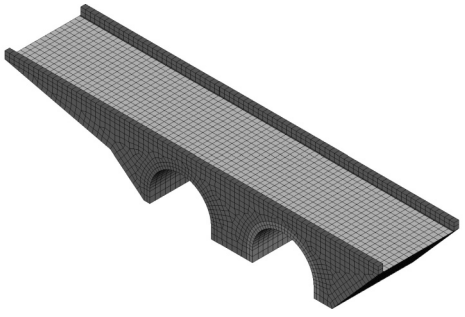

Fig. 6 3D FE mesh of Roman Bridge.

Table 3 Frequency values and direction dependent participation factors for the first five modes of the bridge

mode	frequency values (Hz)	direction dependent participation factors			modal mass (%)
		x direction	*y* direction	*z* direction	
1	9.38	−0.055	938.110	−0.009	15.39
2	11.34	969.080	0.073	−9.381	21.33
3	11.47	−0.237	22.829	−0.014	12.04
4	15.18	0.065	358.830	−0.109	10.53
5	15.44	−23.327	−0.009	105.340	8.28

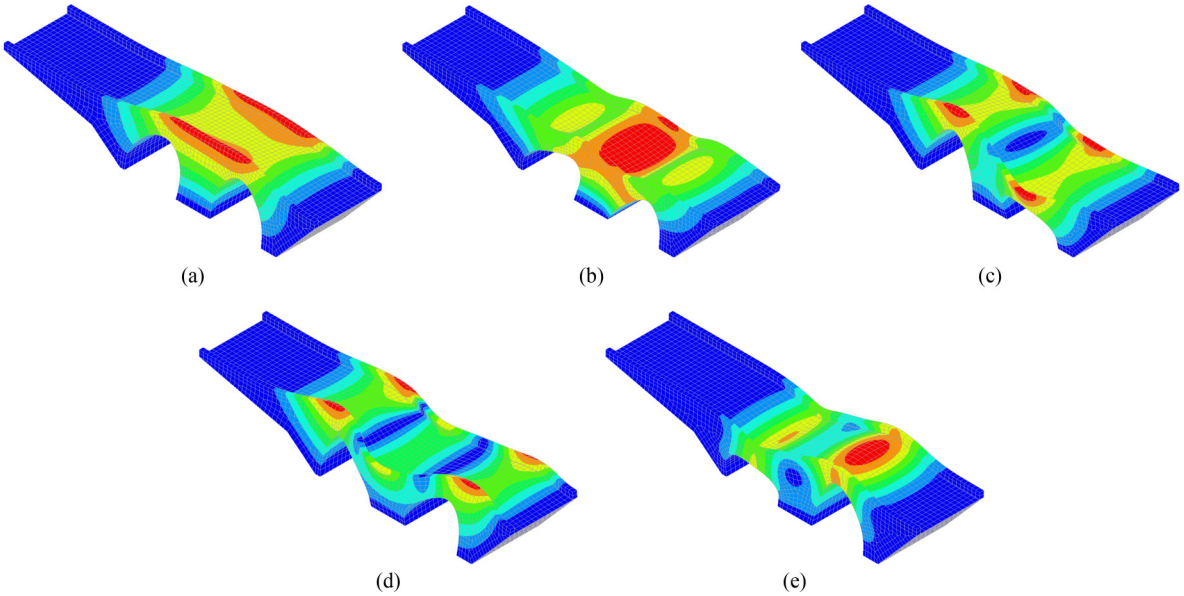

Fig. 7 Natural frequency values (f) and mode shapes of first five modes of developed models: (a) f_1 = 9.38 Hz; (b) f_2 = 11.34 Hz; (c) f_3 = 11.47 Hz; (d) f_4 = 15.18 Hz; (e) f_5 = 15.44 Hz.

Table 3 and Fig. 7 it can be reported that the first, third and fourth modes are in the transverse (y) direction, the second mode is in the longitudinal (x) direction, and the fifth mode is in the vertical (z) direction of the bridge.

A comprehensive experimental study was conducted to investigate the dynamic characteristics of historical masonry arch bridges by performing an operational modal analysis of eight bridges [59]. Equation (2) was proposed to calculate the first frequency value of masonry arch bridges (y) (Hz) based on the maximum arch span (x) (m).

$$y = -3.935\ln x + 16.824. \quad (2)$$

The calculated first natural frequency of the Roman Bridge based on Eq. (2) is 9.46, which is very close to the first natural frequency derived from the modal analysis of the FE models (< 2%). Although Eq. (2) is only based on the span of the bridge by neglecting the effect of material properties and other geometrical characteristics, it shows a good estimation of the first natural frequency value of masonry bridges, as reported in Ref. [60]. However, operational modal analysis based on in situ tests is required to calibrate the model based on the natural frequency values and corresponding mode shapes of the real structure.

5 Performance-based seismic assessment methodology

In this section, earthquake records are selected and scaled to a target response spectrum. NLTHAs are then performed, and the performance level of the bridge is assessed based on a damage index. Finally, a comparative study is performed to investigate the influence of the type of seismic event on the seismic behavior of the structure.

5.1 Earthquake record selection and scaling

In total, 15 seismic events were selected from the PEER NGA-West2 ground-motion database [61]. The flowchart used for selecting seismic events according to different criteria for the three main groups is shown in Fig. 8. Note that the ground type is considered as type B with a shear wave velocity of 360–800 m·s^{-1} [62,63], and the average of the Campbell and Joyner–Boore fault distances was used as the source-to-site distance (*SSD*) [64]. PL-NF event records were chosen based on the method presented in the literature [28] with pulse indicator values > 0.85, early pulses in the time history, and a peak ground velocity (*PGV*) > 30 cm·s^{-1}. The characteristics of the selected seismic records, including the record sequence numbers (*RSN*s) in the PEER database, are presented in Table 4.

All of the selected 15 seismic records were scaled to the target response spectrum [62]. For deriving the target response spectrum, the *PGA* of the island of Rhodes is considered to be 0.47g for soil class B based on the latest seismic hazard map of Europe in the context of the SHARE project [65,66].

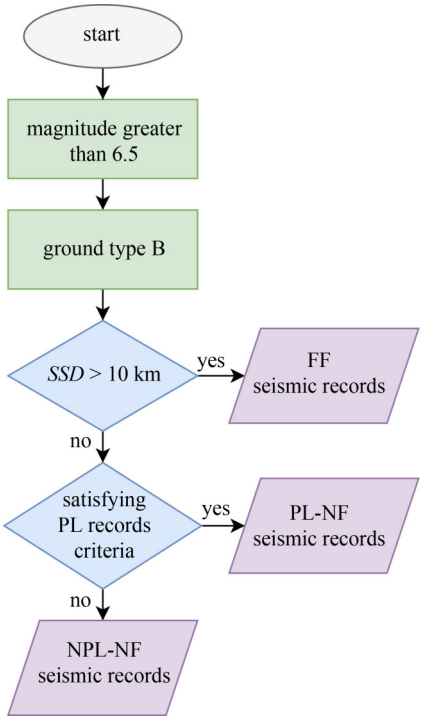

Fig. 8 Flowchart of seismic record selection and categorization.

The bridge is more susceptible in the transverse direction than in the longitudinal direction because the mode shape of the fundamental frequency is in the transverse direction. Moreover, the Northridge seismic record with an intensity of 6.7 M was scaled to a *PGA* of 0.8g and applied to the structure in two directions for preliminary seismic analysis. The results showed that the displacement in the transverse direction of the crown point was ten times greater than that in the longitudinal direction, and the crack width (*CW*) of the model with longitudinal loading was less than that of the model subjected to transverse loading. Therefore, the seismic vulnerability of the bridge was assessed in the transverse direction.

The earthquake records were scaled and matched to the target response spectrum using the SeismoMatch software package [67] in periods from $0.2T_1$–$2T_1$, where T_1 is the fundamental period of the bridge in the transverse direction [62]. An improved scaling method was used to adjust the recorded ground motions without baseline correction [68]. Figure 9(a) shows the single-record spectrum after scaling, and Fig. 9(b) illustrates the mean-matched spectrum.

Five indicators were selected for the scaled seismic

Table 4 Characteristics of selected seismic records [61]

record type	*RSN*	event	station	year	magnitude	*SSD*	*PGA*	*PGV*
FF	313	Corinth, Greece	Corinth	1981	6.6	10.27	0.236	22.955
	3750	Cape Mendocino	Loleta Fire Station	1992	7.01	24.685	0.265	35.525
	1083	Northridge-01	Sunland–Mt Gleason Ave	1994	6.69	12.865	0.132	15.73
	1613	Duzce, Turkey	Lamont 1060	1999	7.14	25.83	0.053	5.755
	1633	Manjil, Iran	Abbar	1990	7.37	12.55	0.514	42.457
PL-NF	828	Cape Mendocino	Petrolia	1992	7.01	4.09	0.590	49.327
	1086	Northridge-01	Sylmar–Olive View Med FF	1994	6.69	3.52	0.604	77.549
	802	Loma Prieta	Saratoga–Aloha Ave	1989	6.93	8.04	0.514	41.579
	879	Landers	Lucerne	1992	7.28	2.19	0.725	133.40
	1013	Northridge-01	LA Dam	1994	6.69	2.96	0.426	74.841
NPL-NF	495	Nahanni, Canada	Site 1	1985	6.76	6.04	1.107	43.926
	825	Cape Mendocino	Cape Mendocino	1992	7.01	3.48	1.493	122.32
	126	Gazli, USSR	Karakyr	1976	6.8	4.69	0.701	66.218
	1004	Northridge-01	LA–Sepulveda VA Hospital	1994	6.69	4.22	0.752	77.673
	741	Loma Prieta	BRAN	1989	6.93	7.285	0.456	51.390

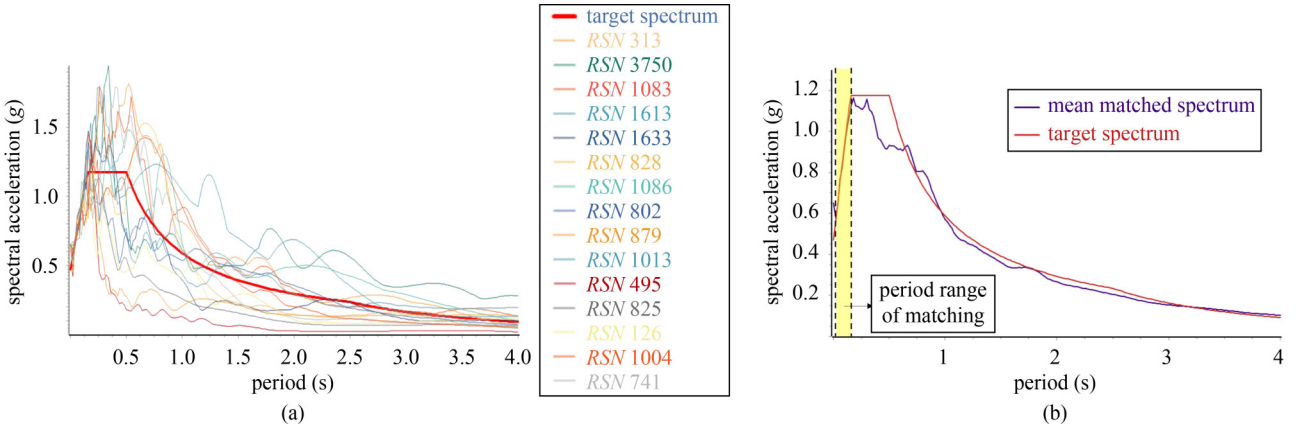

Fig. 9 (a) Seismic records' spectra scaled to the target response spectrum; (b) period range of matching.

records, including *PGA*, *PGV*, Arias intensity (*Ai*), significant duration (*SD*), and specific energy density (*SED*), which are illustrated in Fig. 10, with average values for each group of records. Note that the *Ai* and *SED* are calculated based on:

$$Ai = \frac{\pi}{2g}\int_0^{t_{\max}} [a_{(t)}]^2 \mathrm{d}t, \tag{3}$$

$$SED = \int_0^{t_{\max}} [v_{(t)}]^2 \mathrm{d}t, \tag{4}$$

where $a_{(t)}$ and $v_{(t)}$ are the acceleration and velocity values, respectively, for each time interval, and $t_{\max}$ is the length of the accelerogram. The significant duration is considered as the interval of time in which 5%–95% of the total *Ai* is accumulated [67]. The average values of the *PGA* are close to each other, and the average values of the *PGV* for PL-NF events are closer to the values for FF events and greater than those for the other two types of records. However, the *Ai*, *SED*, and *SD* values of the NF seismic records are less than those of the FF records after scaling.

Scaled seismic event records were applied to the transverse direction of the structure to assess the seismic vulnerability of the bridge, and NLTHAs were performed. Rayleigh damping is used for the models with factors of 3.641 and 0.0006 applied to the mass and stiffness matrices, respectively. Note that the damping factors were calculated by considering a 5% damping ratio for the first and third modes of the bridge models [14,69].

5.2 Seismic performance criteria

Because there are no performance limit states for

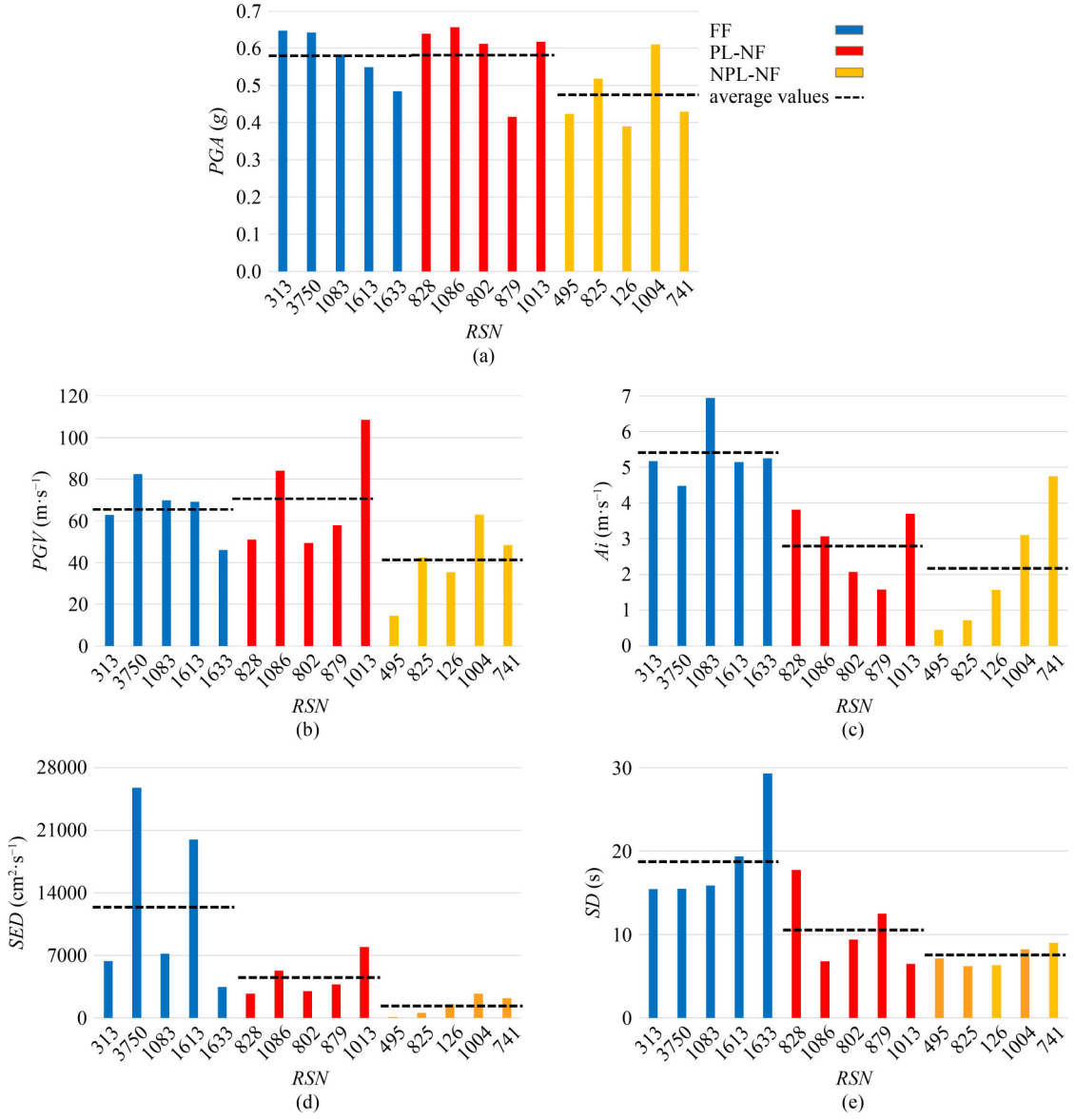

Fig. 10 Scaled seismic event records: (a) *PGA*; (b) *PGV*; (c) *Ai*; (d) *SED*; (e) *SD*.

masonry arch bridges, comprehensive studies are required to define performance criteria. A methodology for determining the quantitative damage criteria for masonry arch bridges was presented in Ref. [70] based on the pushover curve. Three performance levels were considered, and the displacement limit states were determined based on the criteria listed in Table 5. The relationship between the performance levels and the damage states is shown in Fig. 11.

Modal pushover analysis was performed based on the load pattern proportional to the first mode shape [71]. The pushover curves are presented in Fig. 12, by defining the displacement limit states based on the criteria listed in Table 5. The displacement values for the F, LS, and NC limit states are 2.76, 5.78, and 18.5 mm, respectively, as highlighted in Fig. 12. The limit states are derived for the bridge in this study, and a comprehensive study, by developing masonry arch bridges with different geometries, morphologies, and material properties is required to generalize the limit states.

6 Results and discussion

The results for the maximum displacement of the crown point (*Disp*) of the bridge and the three aforementioned limit states are shown in Fig. 13(a). The percentage of the cracked volume of the structure relative to the total volume of the masonry is calculated as a cracked volume damage index (*CVDI*) for each record at the final step of the analysis and illustrated in Fig. 13(b). The *CW*s in the final step of each seismic analysis are shown in Fig. 13(c). Furthermore, the average (Ave) values of the three aforementioned indices are calculated for FF, PL-

Table 5 Performance levels and criteria for determining displacement limit states based on the pushover curve

performance level	functional (F)	life safety (LS)	near collapse (NC)
quantitative description	displacement corresponds to 75% of the maximum base shear (or acceleration)	displacement corresponds to the point on the pushover curve with 7% of the initial (elastic) stiffness	displacement corresponds to 90% of the maximum displacement attained on the pushover curve
qualitative description	structure is mostly elastic with little or no damage; traffic is not interrupted, and damage can be repaired in a couple of days	plasticity starts increasing before and after this performance level; bridge is expected to suffer medium to significant damage; it should still be feasible to repair but cannot be used for a short duration	damage is heavy and distributed to the extent that the bridge is near to collapse state; bridge may even be out-of-service or replaced completely

NF, NPL-NF, and NF events and all event records, as presented in Fig. 13.

By focusing on the response of the bridge to single records, it can be concluded that different damage indices reflect different structural behaviors. The volume of the cracked parts is relatively high for *RSN* 828, but the other two indices are not significantly large. By comparing the seismic behavior of the bridge subjected to *RSN* 3750 and *RSN* 1083, it can be concluded that a higher value of the

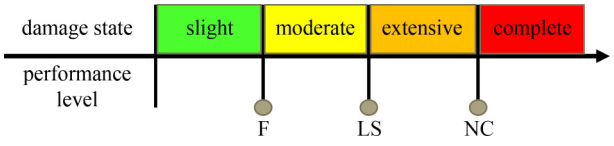

Fig. 11 Relationships between performance levels and damage states.

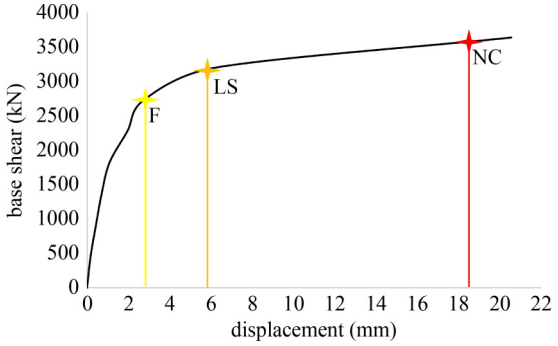

Fig. 12 Pushover curve of the bridge with performance limits.

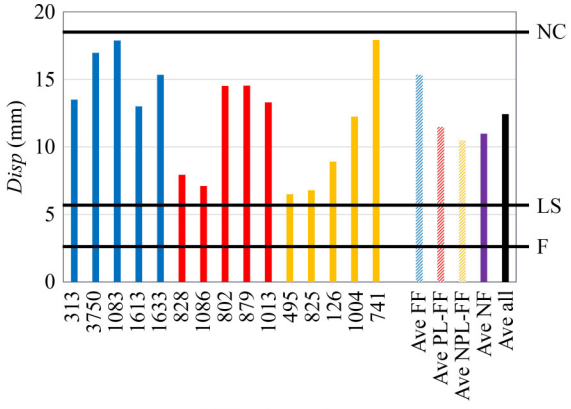

(a)

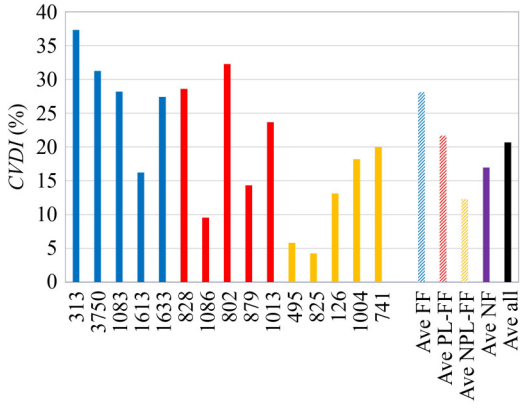

(b)

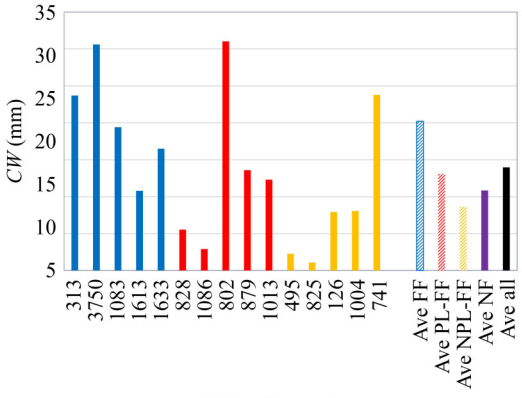

(c)

Fig. 13 Results of NLTHA in terms of: (a) *Disp*; (b) *CVDI*; (c) *CW*.

displacement does not necessarily result in a higher value of the cracked volume damage index and *CW*. Furthermore, the displacement damage index cannot necessarily reflect the seismic damage state of the bridge, and performance level criteria should be defined for the cracked volume damage index and verified based on the experimental tests for stone masonry bridges. As can be seen, some events, such as *RSN* 802 or *RSN* 879 as PL-NF events and *RSN* 741 as an NPL-NF event, have destructive effects on the bridge, similar to FF events. Therefore, it should be noted that it is not sufficiently reliable to perform a comparative study on the effect of earthquake excitation characteristics on the seismic behavior of structures by applying one or two pairs of event records.

The results show that the PL-NF events are more destructive than the NPL-NF excitations. Moreover, more extensive damage occurs to the structure subjected to FF events than NF events. The cracked volume damage index and displacement values of the bridge subjected to PL-NF events were 9.6% and 76.6% higher than those of the bridge subjected to NPL-NF events. Therefore, PL-NF events are more destructive in terms of the cracked volume damage index.

6.1 Regression and correlation analysis

To investigate the correlation between the excitation properties and seismic behavior of the structure in terms of the three damage indices, a linear regression analysis was performed, and the results, including the linear trendline and R^2 values, are presented in Fig. 14. The positive slope of the trend lines reveals that, generally, all parameters have a positive correlation with the damage indices, however, exceptions can also be seen by comparing the characteristics of some seismic records and the corresponding structural demands.

The R^2 values are presented in Fig. 15 on a scale of 0–0.5 to facilitate the comparison. Higher values of R^2 indicate that the change in parameter can explain the change in structural demand in a better way. *Ai* can be a good seismic intensity indicator for predicting the seismic behavior of a bridge in terms of all damage indices.

6.2 Seismic performance evaluation of the bridge

The bridge subjected to seismic events scaled to the target response spectrum with a 10% probability of exceeding it in 50 years with a 475-year return period passed the acceptance criteria for the LS performance level and reported extensive post-earthquake damage. Therefore, the bridge should be repaired after an earthquake; however, this may not be practical for economic reasons. Furthermore, the bridge should be strengthened to prevent future seismic losses.

The applied accelerograms of the *RSN* 1083, *RSN* 1013, and *RSN* 126 events are illustrated in Fig. 16(a) as samples of the FF, PL-NF, and NPL-NF excitations. Figure 16(b) shows the displacement time-history response of the crown point of the bridge subjected to the

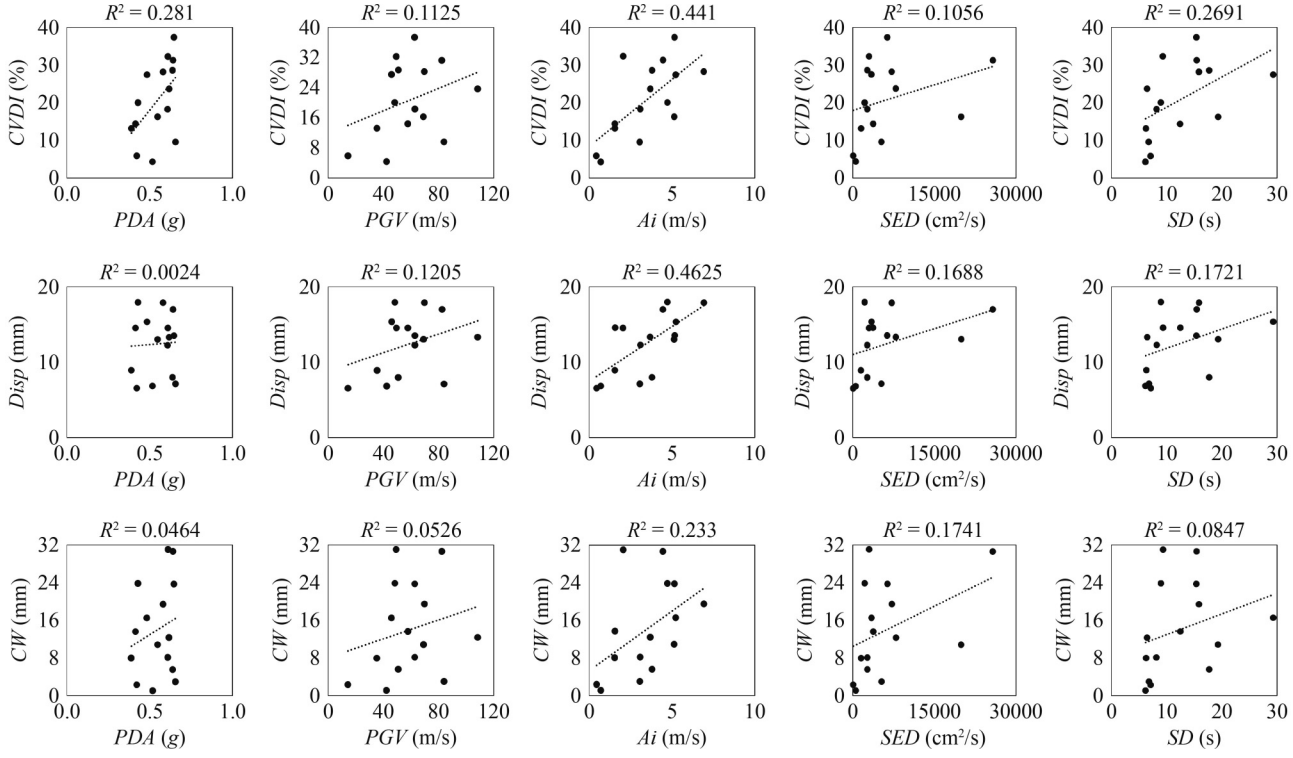

Fig. 14 Trendlines and R^2 values for seismic record properties and structural demands.

selected events. The residual displacements that are presented in Fig. 16(b) are due to the fact that most of the bridge elements were in their plastic phase after applying the selected records. Figure 16(c) shows the magnified deformed shape of the bridge at the end of the analysis time of the *RSN* 1083 event, which is a common shape in almost all simulations. The results revealed that the relative displacement of the crown points of the two spandrel walls increased in the transverse direction by applying the seismic records.

Figure 17 shows the crack pattern and principal crack strain values (E_{knn}) of the model at the final step of analyzing the bridge subjected to the *RSN* 1083, *RSN* 1013, and *RSN* 126 events. The results show that arches are the most susceptible areas, with higher crack strain values than spandrel walls. Cracks can be found in all the models in the arches and close to the spandrel walls, as shown in Fig. 17 for three-sample earthquake records. The area between the arches is the most vulnerable section of the spandrel wall. Therefore, a strategy to strengthen the arches (especially the area close to the spandrel walls) is needed so that the spandrel wall between the two arches can be sufficiently efficient to reduce the seismic vulnerability of the structure.

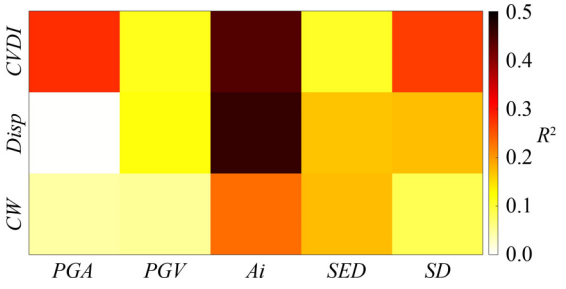

Fig. 15 R^2 values for different seismic record parameters and structural demand.

7 Conclusions

In this study, geometric documentation of the Roman Bridge on the island of Rhodes, in Greece, was performed using advanced digital imaging, 3D laser scanning, and total stations, and the methodology for providing an accurate 3D model was described. Because the bridge is located in a high-seismicity zone, the seismic vulnerability of the bridge also needs to be assessed. Fifteen seismic records were therefore selected based on site specifications and categorized as FF, Pl-NF, or NPL-NF.

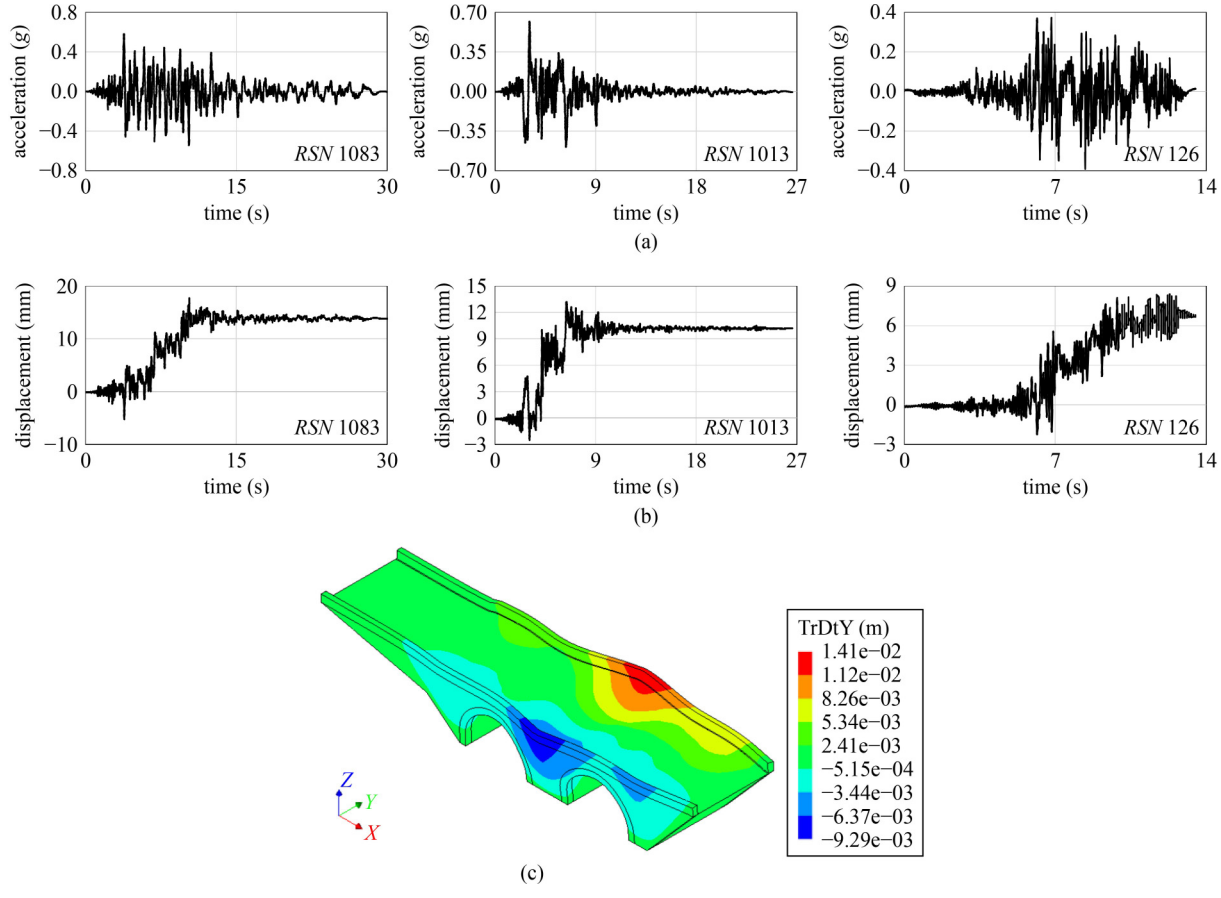

Fig. 16 (a) Accelerograms of *RSN* 1083, *RSN* 1013, and *RSN* 126 events; (b) displacement response time history of the crown points; (c) magnified deformed shape of the bridge subjected to *RSN* 1083 record at the end of the analysis.

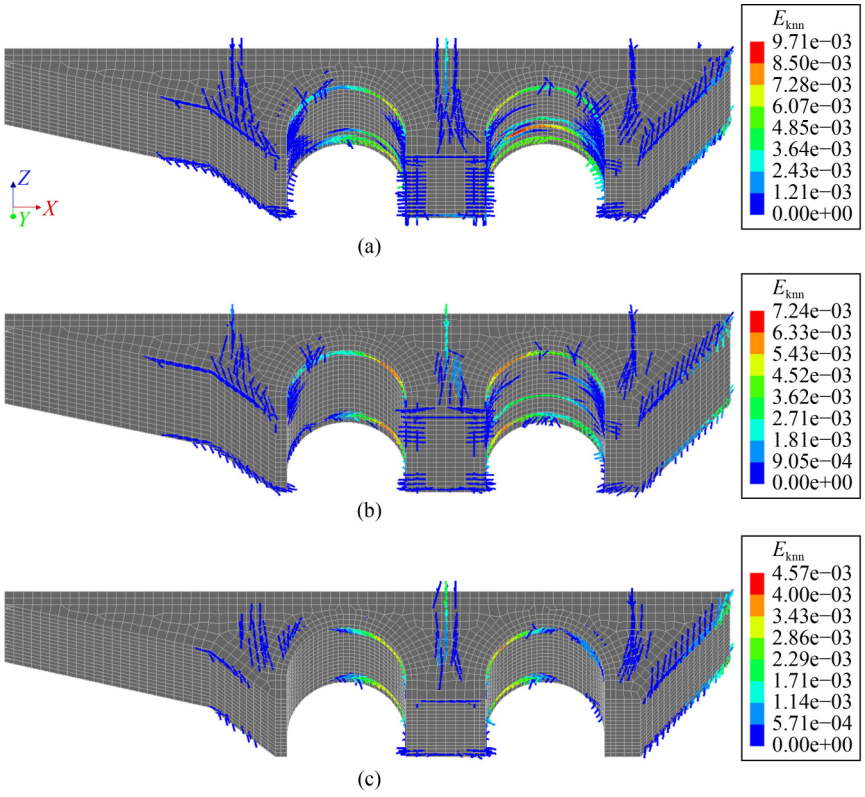

Fig. 17 Crack pattern and principal crack strain values for: (a) *RSN* 1083; (b) *RSN* 1013; (c) *RSN* 126.

The event records were scaled to the target spectrum and applied to the FE model in the transverse direction. The results of the NLTHA revealed that the structure is more susceptible to PL events than to NPL events by comparing the three damage indices. Furthermore, FF events are more destructive than NF events. Linear regression analysis revealed that the *Ai* is the most accurate indicator as one of the seismic records' properties for prediction of the structural demands to different types of excitations. The seismic performance of the bridge was evaluated by defining three performance levels based on the pushover curve. The time-history analysis indicates that the structure passes the acceptability check of the LS performance level and undergoes extensive damage. Temporary wooden scaffolds were built beneath the arches owing to the falling of the stones. Moreover, based on the damage patterns concluded from the numerical analyses, the arches are the most vulnerable structural components, which is consistent with the weakness of the real structure. The observed crack patterns indicate that the structure must be retrofitted by strengthening the arches, focusing on the area close to the spandrel walls and the spandrel wall between the arches. The model should be calibrated based on the operational modal analysis results of the on-site ambient vibration tests, and advanced seismic analyses should be conducted considering soil–structure interaction effects for future studies.

Acknowledgements This work was part of the HYPERION project. HYPERION has received funding from the European Union's Framework Programme for Research and Innovation (Horizon 2020) under grant agreement No. 821054. The contents of this publication are the sole responsibility of the Oslo Metropolitan University (Work Package 5, Task 2) and do not necessarily reflect the opinion of the European Union.

Funding note Open Access funding provided by OsloMet-Oslo Metropolitan University.

Conflict of Interest The authors declare that they have no conflict of interest.

References

1. Khosrowjerdi S, Sarkardeh H, Kioumarsi M. Effect of wind load

on different heritage dome buildings. European Physical Journal Plus, 2021, 136(11): 1180
2. van Beek G W. Arches and vaults in the ancient Near East. Scientific American, 1987, 257(1): 96−103
3. Sarhosis V, de Santis S, de Felice G. A review of experimental investigations and assessment methods for masonry arch bridges. Structure and Infrastructure Engineering, 2016, 12: 1439−1464
4. Gönen S, Soyöz S. Seismic analysis of a masonry arch bridge using multiple methodologies. Engineering Structures, 2021, 226: 111354
5. Shabani A, Kioumarsi M, Zucconi M. State of the art of simplified analytical methods for seismic vulnerability assessment of unreinforced masonry buildings. Engineering Structures, 2021, 239: 112280
6. Yekrangnia M, Mobarake A A. Restoration of historical Al-Askari shrine. II: Vulnerability assessment by numerical simulation. Journal of Performance of Constructed Facilities, 2016, 30(3): 04015031
7. Brencich A, de Francesco U. Assessment of multispan masonry arch bridges. I: Simplified approach. Journal of Bridge Engineering, 2004, 9(6): 582−590
8. de Felice G. Assessment of the load-carrying capacity of multi-span masonry arch bridges using fibre beam elements. Engineering Structures, 2009, 31(8): 1634−1647
9. de Santis S, de Felice G. A fibre beam-based approach for the evaluation of the seismic capacity of masonry arches. Earthquake Engineering & Structural Dynamics, 2014, 43(11): 1661−1681
10. Audenaert A, Fanning P, Sobczak L, Peremans H. 2-D analysis of arch bridges using an elasto-plastic material model. Engineering Structures, 2008, 30(3): 845−855
11. Zampieri P, Zanini M A, Faleschini F, Hofer L, Pellegrino C. Failure analysis of masonry arch bridges subject to local pier scour. Engineering Failure Analysis, 2017, 79: 371−384
12. Fanning P, Sobczak L, Boothby T E, Salomoni V. Load testing and model simulations for a stone arch bridge. Bridge Structures, Assessment, Design and Construction, 2005, 1: 367−378
13. Milani G, Lourenco P B. 3D non-linear behavior of masonry arch bridges. Computers & Structures, 2012, 110: 133−150
14. Hokelekli E, Yilmaz B N. Effect of cohesive contact of backfill with arch and spandrel walls of a historical masonry arch bridge on seismic response. Periodica Polytechnica. Civil Engineering, 2019, 63: 926−937
15. Bayraktar A, Hökelekli E. Seismic performances of different spandrel wall strengthening techniques in masonry arch bridges. International Journal of Architectural Heritage, 2021, 15(11): 1722−1740
16. Banerji P, Chikermane S. Condition assessment of a heritage arch bridge using a novel model updation technique. Journal of Civil Structural Health Monitoring, 2012, 2(1): 1−16
17. Zampieri P, Tetougueni C D, Pellegrino C. Nonlinear seismic analysis of masonry bridges under multiple geometric and material considerations: Application to an existing seven-span arch bridge. Structures, 2021, 34: 78−94
18. van Langen H, Vermeer P. Interface elements for singular plasticity points. International Journal for Numerical and Analytical Methods in Geomechanics, 1991, 15(5): 301−315
19. Herrmann L R. Finite element analysis of contact problems. Journal of the Engineering Mechanics Division, 1978, 104(5): 1043−1057
20. Zhang S, Wang G. Effects of near-fault and far-fault ground motions on nonlinear dynamic response and seismic damage of concrete gravity dams. Soil Dynamics and Earthquake Engineering, 2013, 53: 217−229
21. Pang Y T, Cai L, Zhong J. Seismic performance evaluation of fiber-reinforced concrete bridges under near-fault and far-field ground motions. Structures, 2020, 28: 1366−1383
22. Yekrangnia M, Bakhshi A, Ghannad M A, Panahi M. Risk assessment of confined unreinforced masonry buildings based on FEMA P-58 methodology: A case study—School buildings in Tehran. Bulletin of Earthquake Engineering, 2021, 19(2): 1079−1120
23. Sevim B, Atamturktur S, Altunişik A C, Bayraktar A. Ambient vibration testing and seismic behavior of historical arch bridges under near and far fault ground motions. Bulletin of Earthquake Engineering, 2016, 14(1): 241−259
24. Simos N, Manos G C, Kozikopoulos E. Near- and far-field earthquake damage study of the Konitsa stone arch bridge. Engineering Structures, 2018, 177: 256−267
25. Güllü H, Özel F. Microtremor measurements and 3D dynamic soil–structure interaction analysis for a historical masonry arch bridge under the effects of near- and far-fault earthquakes. Environmental Earth Sciences, 2020, 79(13): 338
26. Özmen A, Sayın E. Seismic response of a historical masonry bridge under near and far-fault ground motions. Periodica Polytechnica Civil Engineering, 2021, 65: 946−958
27. Labbé P, Altinyollar A. Conclusions of an IAEA–JRC research project on the safety significance of near-field seismic motions. Nuclear Engineering and Design, 2011, 241(5): 1842−1856
28. Baker J W. Quantitative classification of near-fault ground motions using wavelet analysis. Bulletin of the Seismological Society of America, 2007, 97(5): 1486−1501
29. Shahi S K, Baker J W. An efficient algorithm to identify strong-velocity pulses in multicomponent ground motions. Bulletin of the Seismological Society of America, 2014, 104(5): 2456−2466
30. Chang Z, Sun X, Zhai C, Zhao J X, Xie L. An improved energy-based approach for selecting pulse-like ground motions. Earthquake Engineering & Structural Dynamics, 2016, 45(14): 2405−2411
31. Dimakopoulou V, Fragiadakis M, Taflampas I. A wavelet-based approach for truncating pulse-like records. Bulletin of Earthquake Engineering, 2022, 20(1): 1−24
32. Daei A, Poursha M, Zarrin M. Seismic performance evaluation of code-compliant RC moment-resisting frame buildings subjected to near-fault pulse-like and non-pulse-like ground motions. Journal of Earthquake Engineering, 2021, 26(10): 5058−5085
33. Zuo Z, Gong M, Sun J, Zhang H. Seismic performance of RC frames with different column-to-beam flexural strength ratios under the excitation of pulse-like and non-pulse-like ground motion. Bulletin of Earthquake Engineering, 2021, 19(12): 5139−5159
34. Wibowo H, Sritharan S. Effects of vertical ground acceleration on the seismic moment demand of bridge superstructure connections.

Engineering Structures, 2022, 253: 113820
35. Kohrangi M, Vamvatsikos D, Bazzurro P. Pulse-like versus non-pulse-like ground motion records: Spectral shape comparisons and record selection strategies. Earthquake Engineering & Structural Dynamics, 2019, 48(1): 46−64
36. Orfeo B, Todisco L, León J. Construction process of vaults in masonry bridges: The importance of centrings. International Journal of Architectural Heritage, 2022, 16(7): 1032−1046
37. Gençer F U, Turan M H. The masonry techniques of a historical bridge in Hypokremnos (İçmeler). Metu Journal of the Faculty of Architecture, 2017, 34(1): 187−207
38. Pagani M, Garcia-Pelaez J, Gee R, Johnson K, Poggi V, Silva V, Simionato M, Styron R, Viganò D, Danciu L, Monelli D, Weatherill G. The 2018 version of the global earthquake model: Hazard component. Earthquake Spectra, 2020, 36(1_suppl): 226−251
39. Stiros S, Papageorgiou S, Kontogianni V, Psimoulis P. Church repair swarms and earthquakes in Rhodes Island, Greece. Journal of Seismology, 2006, 10(4): 527−537
40. Howell A, Jackson J, England P, Higham T, Synolakis C. Late Holocene uplift of Rhodes, Greece: Evidence for a large tsunamigenic earthquake and the implications for the tectonics of the eastern Hellenic Trench System. Geophysical Journal International, 2015, 203(1): 459−474
41. Shabani A, Alinejad A, Teymouri M, Costa A N, Shabani M, Kioumarsi M. Seismic vulnerability assessment and strengthening of heritage timber buildings: A review. Buildings, 2021, 11(12): 661
42. Tapinaki S, Skamantzari M, Anastasiou A, Koutros S, Syrokou E, Georgopoulos A. 3D holistic documentation of heritage monuments in Rhodes. The International Archives of the Photogrammetry, Remote Sensing and Spatial Information Sciences, 2021, XLVI-M-1-2021: 739−744
43. Kolokoussis P, Skamantzari M, Tapinaki S, Karathanassi V, Georgopoulos A. 3D and hyperspectral data integration for assessing material degradation in medieval masonry heritage buildings. The International Archives of the Photogrammetry, Remote Sensing and Spatial Information Sciences, 2021, XLIII-B2-2021: 583−590
44. Shabani A, Skamantzari M, Tapinaki S, Georgopoulos A, Plevris V, Kioumarsi M. 3D simulation models for developing digital twins of heritage structures: Challenges and strategies. Procedia Structural Integrity, 2022, 37: 314−320
45. DIANA. Version 10.4. Delft: DIANA FEA BV. 2020
46. Plevris V, Asteris P G. Modeling of masonry failure surface under biaxial compressive stress using Neural Networks. Construction & Building Materials, 2014, 55: 447−461
47. D'Altri A M, Sarhosis V, Milani G, Rots J, Cattari S, Lagomarsino S, Sacco E, Tralli A, Castellazzi G, de Miranda S. Modeling strategies for the computational analysis of unreinforced masonry structures: Review and classification. Archives of Computational Methods in Engineering, 2020, 27(4): 1153−1185
48. Asteris P G, Chronopoulos M P, Chrysostomou C Z, Varum H, Plevris V, Kyriakides N, Silva V. Seismic vulnerability assessment of historical masonry structural systems. Engineering Structures, 2014, 62–63: 118–134
49. Asteris P G, Sarhosis V, Mohebkhah A, Plevris V, Papaloizou L, Komodromos P, Lemos J V. Numerical modeling of historic masonry structures. In: Asteris P G, Plevris V, eds. Handbook of Research on Seismic Assessment and Rehabilitation of Historic Structures. Hershey, PA: IGI Global, 2015, 213–256
50. Kioumarsi M, Plevris V, Shabani A. Vulnerability assessment of cultural heritage structures. In: The 8th European Congress on Computational Methods in Applied Sciences and Engineering (ECCOMAS 2022). Oslo: Scipedia, 2022, C52
51. Fanning P J, Boothby T E. Three-dimensional modelling and full-scale testing of stone arch bridges. Computers & Structures, 2001, 79(29−30): 2645−2662
52. Aytulun E, Soyoz S, Karcioglu E. System identification and seismic performance assessment of a stone arch bridge. Journal of Earthquake Engineering, 2022, 26(2): 723−743
53. Wang J. Numerical modelling of masonry arch bridges: Investigation of spandrel wall failure. Dissertation for the Doctoral Degree. Bath: University of Bath, 2014
54. Selby R G. Three-dimensional constitutive relations for reinforced concrete. Dissertation for the Doctoral Degree. Toronto: University of Toronto, 1993
55. Rots J G. Computational modeling of concrete fracture. Dissertation for the Doctoral Degree. Delft: Delft University of Technology, 1988
56. Psycharis I N, Avgenakis E, Taflampas I M, Kroustallaki M, Farmakidou E, Pikoula M, Michailidou M, Moropoulou A. Seismic response of the Temple of Pythian Apollo in Rhodes Island and recommendations for its restoration. In: Osman A, Moropoulou A, eds. Nondestructive Evaluation and Monitoring Technologies, Documentation, Diagnosis and Preservation of Cultural Heritage. Berlin: Springer, 2019, 160–177
57. Ghiassi B, Vermelfoort A T, Lourenço P B. Chapter 7—Masonry mechanical properties. In: Ghiassi B, Milani G, eds. Numerical Modeling of Masonry and Historical Structures. Sawston: Woodhead Publishing, 2019, 239–261
58. Forgács T, Rendes S, Ádány S, Sarhosis V. Mechanical role of spandrel walls on the capacity of masonry arch bridges. In: Proceedings of ARCH 2019. Berlin: Springer, 2020, 221–229
59. Bayraktar A, Türker T, Altunişik A C. Experimental frequencies and damping ratios for historical masonry arch bridges. Construction & Building Materials, 2015, 75: 234−241
60. Onat O. Impact of mechanical properties of historical masonry bridges on fundamental vibration frequency. Structures, 2020, 27: 1011−1028
61. PEER. PEER Ground Motion Database. Berkeley, CA: University of California, 2021
62. EN 1998-1. Eurocode 8: Design of Structures for Earthquake Resistance-Part 1: General Rules, Seismic Actions and Rules for Buildings. Brussels: European Committee for Standardization, 2004
63. Karatzetzou A, Pitilakis D, Karafagka S. System identification of mosques resting on soft soil. The case of the Suleiman Mosque in the Medieval City of Rhodes, Greece. Geosciences, 2021, 11(7): 275
64. FEMA P695. Quantification of Building Seismic Performance Factors. Washington, D.C.: Federal Emergency Management

Agency, 2009

65. Giardini D, Wössner J, Danciu L. Mapping Europe's seismic hazard. Eos, Transactions American Geophysical Union, 2014, 95(29): 261−262
66. Pitilakis K, Riga E, Roumelioti Z. The urgent need for an improvement of the Greek seismic code based on a new seismic hazard map for Europe and a new site classification system. In: Kavvadas M, ed. Jubilee Volume, Andreas Anagnostopoulos, 50 Years of Service at The National Technical University of Athens. Athens: Tsotras, 2016, 437–461
67. SeismoMatch: Earthquake software for response spectrum matching. Version 2021. Pavia: SeismoSoft–Earthquake Engineering Software Solutions. 2021
68. Al Atik L, Abrahamson N. An improved method for nonstationary spectral matching. Earthquake Spectra, 2010, 26(3): 601−617
69. Bertolesi E, Milani G, Lopane F D, Acito M. Augustus Bridge in Narni (Italy): Seismic vulnerability assessment of the still standing part, possible causes of collapse, and importance of the Roman concrete infill in the seismic-resistant behavior. International Journal of Architectural Heritage, 2017, 11(5): 717−746
70. Gönen S, Soyöz S. Reliability-based seismic performance of masonry arch bridges. Structure and Infrastructure Engineering, 2022, 18(12): 1658−1673
71. Chopra A K, Goel R K. A modal pushover analysis procedure for estimating seismic demands for buildings. Earthquake Engineering & Structural Dynamics, 2002, 31(3): 561−582